

CrossMark
click for updatesCite this: *RSC Adv.*, 2016, 6, 67184

Tunable bioelectrodes with wrinkled-ridged graphene oxide surfaces for electrochemical nitrate sensors†

Md. Azahar Ali,^a Wei Hong,^b Seval Oren,^a Qiugu Wang,^a Yifei Wang,^a Huawei Jiang^a and Liang Dong^{*a}

The paper reports on controlled formation of microscale wrinkles and ridges on the surface of a bioelectrode *via* mechanical stretching to tune and optimize the electrochemical sensing performances of graphene oxide (GO) based nitrate ion sensors. The bioelectrode consists of GO nanosheets drop-coated on a gold (Au) layer with a pre-stretched elastomer substrate. Enzyme nitrate reductase is used for covalent immobilization on the wrinkled-ridged GO surface. Upon relaxation from the pre-stretch, wrinkles or ridges are formed in the GO layer. As the pre-stretch increases, the sinusoidal wrinkles transform to localized ridges on the surface of bioelectrodes. Such morphological transitions, realized by simple mechanical stretching and relaxing, allow optimizing of the electrochemical current and sensing characteristics of the nitrate sensor. The sensing performances of the bioelectrodes at different pre-stretches are investigated. In addition to an increased electroactive surface area, the predominant localized ridges with small sinusoidal wrinkles formed on the GO surface provide a favorable spatial feature, enabling efficient radial diffusion of nitrate ions from surrounding analyte solutions onto the surface of the textured bioelectrode. At the pre-stretch of 8%, the nitrate sensor using the wrinkled-ridged bioelectrode exhibits a considerably high sensitivity of 0.224 $\mu\text{A L mol}^{-1} \text{cm}^{-2}$ in response to nitrate ions, which is five times higher than that provided by the planar counterpart. Also, the textured bioelectrode shows high selectivity even in the presence of other interfering ions. The present nitrate sensor has potential applications in nitrate detection in sustainable agriculture, environmental monitoring, food analysis, and pharmaceutical industries.

Received 13th April 2016

Accepted 10th July 2016

DOI: 10.1039/c6ra09621b

www.rsc.org/advances

1. Introduction

High-sensitivity, high-selectivity monitoring of nitrate ions (NO_3^-) with inexpensive portable devices is highly appealing for a vast variety of applications, including in sustainable agriculture, environmental monitoring, food analysis, and pharmaceutical industries.^{1–4} Extensive use of nitrate fertilizers in agriculture has negatively impacted ground water, soil, and marine ecosystems. The presence of enriched nitrate ions in food products also has a potential human health threat. Common practice for nitrate detection includes using ion exchange chromatography, spectrophotometry,⁵ colorimetric sensors,⁶ ion-selective electrodes, and ion-sensitive field effect transistors. Due to its high signal-to-noise ratio and low limit-of-detection, electrochemical means of nitrate detection has been in high demand, which often relies on using different sensitive

materials, such as methyl viologen/Nafion,¹ polypyrrole,² hydrophilic poly(pyrrole-viologen),³ 1-methyl-3-(pyrrol-1-yl-methyl)pyridinium microporous membrane,⁴ CNT-poly-pyrrole,⁷ polypyrrole,⁸ platinum-tin,⁹ and silver particle-poly-methacrylic-acid.¹⁰ Despite these efforts, there is still much room to improve sensitivity, operational stability, and/or anti-fouling capability for nitrate sensors.^{1,2}

Graphene and graphene oxide (GO) have shown great potential in many research areas, including point-of-care diagnostics or therapeutics,^{11,12} microelectronics,^{13,14} optoelectronics,¹⁵ sensors,¹⁶ and energy storage,¹⁷ due to various attractive properties, such as large surface area, high mechanical strength, high integer quantum Hall effect, and ballistic conduction of charge carriers.¹⁸ By varying pore size, geometry, surface area, and functional sites through structural and morphological transformation of GO, it is possible to tune electrical, chemical, and mechanical properties of GO to meet the needs of specific applications.^{19–21} Single-layer GO nanosheets are known to contain several oxygen-containing groups (*e.g.*, epoxy and hydroxyl) at the basal plane, and carboxyls and ring lactols groups at the edges of GO nanosheets.^{22,23} Since these abundant binding sites can form strong covalent bonds

^aDepartment of Electrical and Computer Engineering, Iowa State University, Ames, IA, 50011, USA. E-mail: ldong@iastate.edu; Tel: +515-294-0388

^bDepartment of Aerospace Engineering, Iowa State University, Ames, IA, 50011, USA

† Electronic supplementary information (ESI) available. See DOI: 10.1039/c6ra09621b

with proteins, enzymes, antibodies, and nucleotides *via* amidation reaction,²⁴ many chemical and biological sensors, such as paracetamol sensors,²⁵ rotavirus sensors,²² and tuberculosis sensors,²³ have been realized utilizing the interactive oxygen framework in GO nanosheets. Also, GO nanosheets provide large amounts of open graphitic edge planes with high surface reactivity, thus offering a promising nanostructured material for electrochemical biosensors.^{26,27} Recently, self-assembled free-standing, graphene–Nafion nanohybrids have been developed to form flexible biosensors for organophosphate detection, which excel in high conductivity, electron transfer, and low interfacial resistance.²⁷ An amperometric nitrate sensor was realized using a reduced GO modified glassy carbon electrode.²⁸

Wrinkled electrophoretic deposited graphene film has been developed for electrochemical detection of explosive compounds.²⁹ In addition, vertical multilayer graphene nanosheets have demonstrated fast electron-transfer kinetics and good electrocatalytic activity to monitor dopamine, ascorbic acid, and uric acid.³⁰

In recent years, surface wrinkling of a stiff thin film supported by a compliant thick substrate has received much attention.^{31,32} Under a critical strain, the surface of the film loses the stability and forms different wrinkle morphologies, such as sinusoidal, herringbone, checkerboard, and hexagonal modes due to different uniaxial to biaxial compression.^{33,34} Although conventional photolithography and micromachining methods can

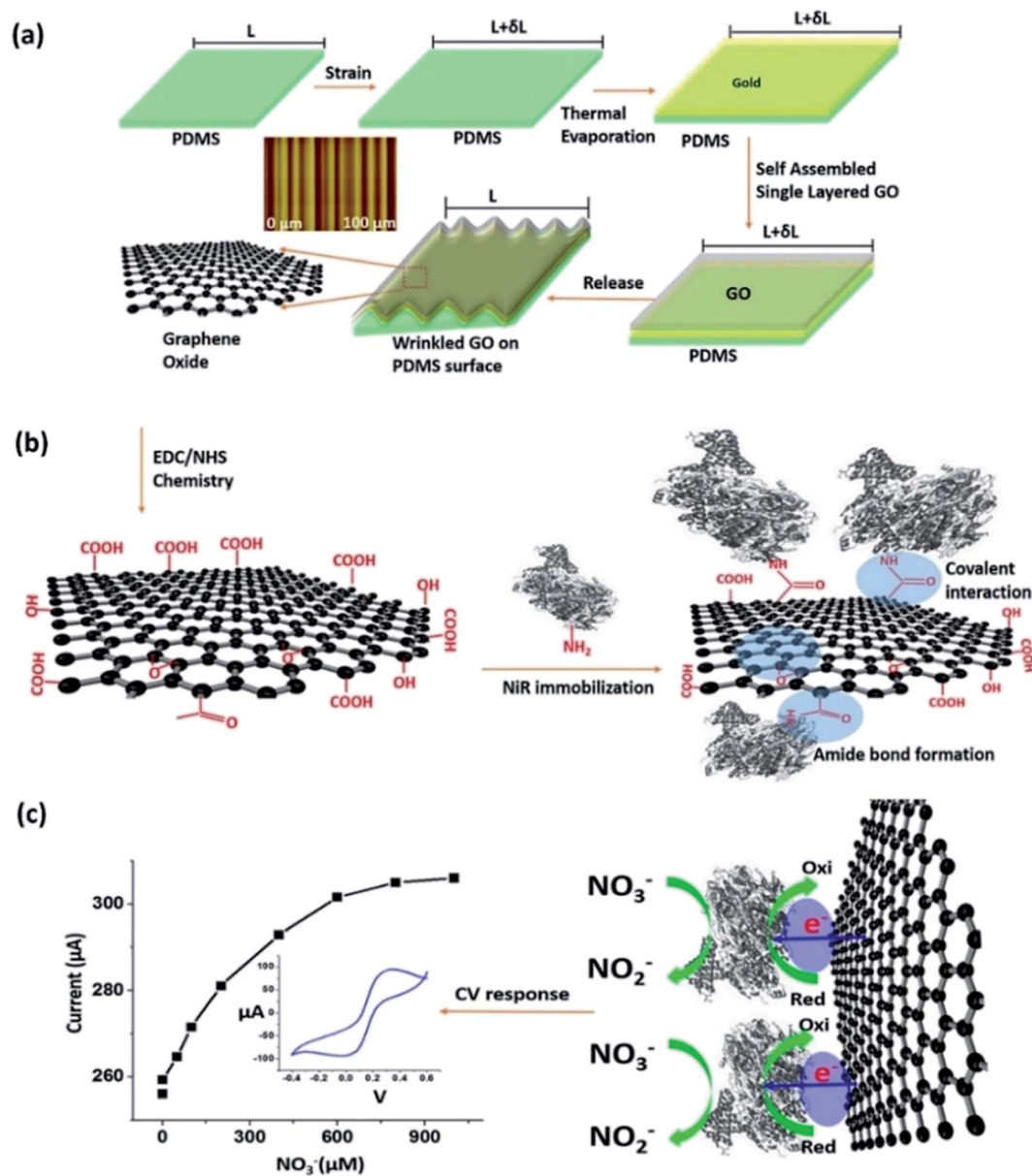


Fig. 1 Pictorial representation of the nitrate sensor using a GO–Au bioelectrode with a wrinkled and/or ridged surface. (a) Method of forming wrinkles and/or ridges. (b) Surface functionalization of enzyme molecules. (c) Sensing mechanism and typical electrochemical responses of the sensor to different nitrate ion concentrations.

produce similar patterns, using the strain based method to stimulate surface wrinkles is of low cost.^{31,32} Several applications of wrinkling surfaces have been investigated, such as forming self-assembly ordered microstructures, microfluidic channels, cell alignment, liquid crystal displays, and diffraction gratings.^{35–37}

Here we report on tunable electrochemical bioelectrodes with controlled formation of wrinkled and ridged in GO layer for detecting nitrate ions with optimized sensing performances. Different wrinkles and ridges at the microscale are formed on the surface of GO by simply adjusting pre-stretch on an elastomer substrate (polydimethylsiloxane or PDMS) prior to sequential evaporation of a gold (Au) thin film, drop coating of single-layer GO nanosheets, and relaxation from the GO–Au–PDMS composite (Fig. 1a). With increasing pre-stretch, morphological transitions from sinusoidal wrinkles to localized ridges occur at the surface of the composite. This allows tuning surface texture of GO for enzyme immobilization to form a tunable electrochemical bioelectrode. Compared to the planar counterpart bioelectrode, the present GO-based bioelectrode with wrinkles and ridges can provide not only a larger surface area, but also a higher ion diffusivity due to radial diffusion. To realize selective detection of nitrate ions, nitrate reductase (NiR) enzyme is immobilized on the wrinkled GO surface *via* EDC–NHS coupling chemistry (Fig. 1b). This recognition element is conjugated with GO nanosheets and reacts with nitrate ions *via* reduction of nitrate to nitrite, producing electrons through catalytic conversion of the enzymatic reaction, resulting in an increased electrochemical current (Fig. 1c). Our experiment demonstrates that the controlled formation of wrinkles and ridges on the surface of bioelectrode allows tuning the sensing performances of GO-based nitrate sensors. The result also shows that the predominant localized ridges with small sinusoidal wrinkles on the GO surface provide a favorable spatial feature to facilitate radial diffusion of nitrate ions from surrounding analyte solutions onto the surface of bioelectrode, thereby enhancing sensitivity of the sensor.

2. Experimental section

2.1. Materials

The lyophilized powder of nitrate reductase (from *Aspergillus niger*), potassium nitrate (KNO₃), *N*-hydroxysuccinimide (NHS) and *N*-ethyl-*N*-(3-dimethylaminopropyl) carbodiimide (EDC) were purchased from Sigma Aldrich, USA. Single layer GO nanosheets (prepared by the modified Hummer's method; diameter: 0.5–5 μm; thickness: 1–3 nm) were purchased from ACS Material, USA. The elemental compositions in GO are 0%, 40.78%, and 51.26% for N (wt%), O (wt%) and C (wt%), respectively, and the C/O atomic ratio is 1.67.

2.2. Formation of wrinkles and localized ridges on elastomer substrate

Before applying pre-stretch, 1 mm thick PDMS substrates were prepared by mixing PDMS oligomer and curing agent at the weight ratio of 10 : 1, followed by degassing and curing at 90 °C on a hotplate for 2 h. They were then unidirectionally stretched

by applying different strain values (0%, 2.7%, 5.1%, and 8%) using a homemade stretcher (Fig. S1, ESI†). Subsequently, a 5 nm thick titanium (adhesive layer) and a 50 nm thick Au layer were sequentially evaporated onto the pre-stretch PDMS substrate *via* e-beam evaporation (Fig. 1a).³⁸ After that, the surface of Au substrates were treated by oxygen plasma. In this process, the hydrophobic nature of the Au surface become hydrophilic. Also, various residuals including organic impurities and weakly bound organic contaminants were removed from the Au surface. A well-dispersed colloidal solution of single-layer GO nanosheets (0.4 mg mL⁻¹) was prepared in deionized (DI) water (Millipore water purification system) *via* thorough sonication. 150 μL of this solution was drop cast onto the treated Au surface and dried in air at room temperature for 2 h. Upon relaxation from the pre-stretched PDMS substrate, wrinkles and/or ridges appeared on the surface of the composite. The footprint area of each electrode was 7 mm × 7 mm.

2.3. Surface functionalization

To immobilize NiR enzyme on the surface of the GO modified electrodes, EDC–NHS coupling chemistry was used. The prepared electrodes were treated with EDC–NHS for 4 h to activate functional groups (–COOH) on the GO nanosheets. In EDC–NHS coupling chemistry, the EDC (0.2 M) works as a coupling agent while NHS (0.05 M) works as an activator. This chemical treatment allows for the binding of GO–Au–PDMS and NiR (enzymes) *via* amidation reaction (forming covalent amide bond; C–N) on GO surface. 20 μL volume of NiR solution (3.5 mg mL⁻¹) was spread on the GO surface. We conducted cyclic voltammetry (CV) studies to optimize the amount of NiR enzymes covalently immobilized on the fabricated electrodes. The enzyme solution was varied from 5 to 25 μL for the immobilization on the surface of electrode at the pre-stretch of 8.0%. The maximum peak current was obtained at 20 μL volume of enzyme solution after which it became saturated. With the wrinkles and ridges on the bioelectrode at the pre-stretch of 8.0%, the peak current increased with increasing volume of enzyme molecules due perhaps to favorably oriented enzymes, which may provide more enzyme active sites for catalytic conversion with nitrate ions (Fig. S2, ESI†). The electrodes were then stored for 12 h under 100% relative humidity condition at 4 °C, followed by washing with a phosphate buffered saline (PBS) solution in order to remove any unbound enzymes molecules on the surface. The amide (C–N) bond formation between –COOH groups of GO–Au and –NH₂ groups of NiR enzyme may provide better immobilization compared to physical adsorption *via* electrostatic interaction (Fig. 1). The prepared bioelectrodes were stored at 4 °C when not in use. For the electrochemical studies, the bioelectrodes were immersed in a PBS solution containing ferro/ferri cyanide as a mediator. Fig. 1b and c show the immobilization of NiR enzyme with wrinkled and ridged GO and detection principle of nitrate ions.

2.4. Instrumentation

The GO–Au–PDMS electrodes functionalized with enzyme were confirmed by FTIR (Model IFS 66v/S; Bruker, USA). The surface

morphology was characterized by FE-SEM (Quanta-250; FEI, Hillsboro, OR, USA) and AFM (Veeco, Nanoscope 3D, USA). Raman microscope (Thermo Scientific, Waltham, MA, USA) was used for Raman spectra acquisition with 532 nm excitation at 10 mW, 10 \times objective, and 50 μ m slit. The CV was performed using a potentiostat (Model: DY2100; Digi-Ivy, TX, USA). Homemade Pt and Ag/AgCl electrodes were used for counter and reference electrodes, respectively.

2.5. Modeling of surface morphology

To understand the evolution of the surface morphology, a series of finite-element simulation was carried out with the commercial software SIMULIA Abaqus 6.12. A tri-layer film–substrate system was developed in the 2D rectangular domain. In the numerical calculations, all lengths were normalized by the thickness of the graphene film h , and all stresses by the initial shear modulus of the PDMS substrate, μ_s . The thickness of the Au layer was taken to be $5h$, while that of the PDMS substrate was $400h$. Symmetric boundary conditions were prescribed on the left and right edges. The width of the entire domain measures $3000h$ before deformation. Within the small strain of interest, the graphene film was considered to be linear elastic with Young's modulus $E_g = 5 \times 10^5 \mu_s$ and Poisson's ratio $\nu_g = 0.2$. The PDMS substrate was modeled as an incompressible neo-Hookean material. The Au layer was modeled as elastic-

perfectly-plastic, with Young's modulus $E_{Au} = 3.9 \times 10^4 \mu_s$, Poisson's ratio $\nu_{Au} = 0.42$, and yield strength $S_{Au} = 400 \mu_s$. When a representative value of the PDMS modulus $\mu_s \sim 2$ MPa was taken, the corresponding material parameters, $E_g \sim 1$ GPa, $E_{Au} \sim 78$ GPa, and $E_{Au} \sim 800$ MPa, are all within the range commonly known for these materials. It should be noted that the yield strength of Au films are known to be higher than that of the bulk.

3. Results and discussion

3.1. Formation and morphological studies of wrinkled-ridged surfaces

Fig. 1 shows the fabrication process for the wrinkled and/or ridged electrodes with the pre-stretch values of 0%, 2.7%, 5.1%, and 8%. To investigate surface profiles of the electrodes formed under the different pre-stretch conditions, we performed atomic force microscopy (AFM) and field emission scanning electron microscopy (FESEM) studies. The sinusoidal wave wrinkles were observed (Fig. 2a–c) at the low pre-stretch of 2.7% and their average amplitude (peak-to-peak) and wavelength were found to be ~ 40 nm and ~ 2.5 μ m, respectively. At the higher pre-stretch of 5.1%, the sinusoidal wrinkles were converted to localized ridges (Fig. 2d–f), with an increased average amplitude and wavelength at ~ 390 nm and ~ 11 μ m, respectively. Further, with increasing pre-stretch to 8%

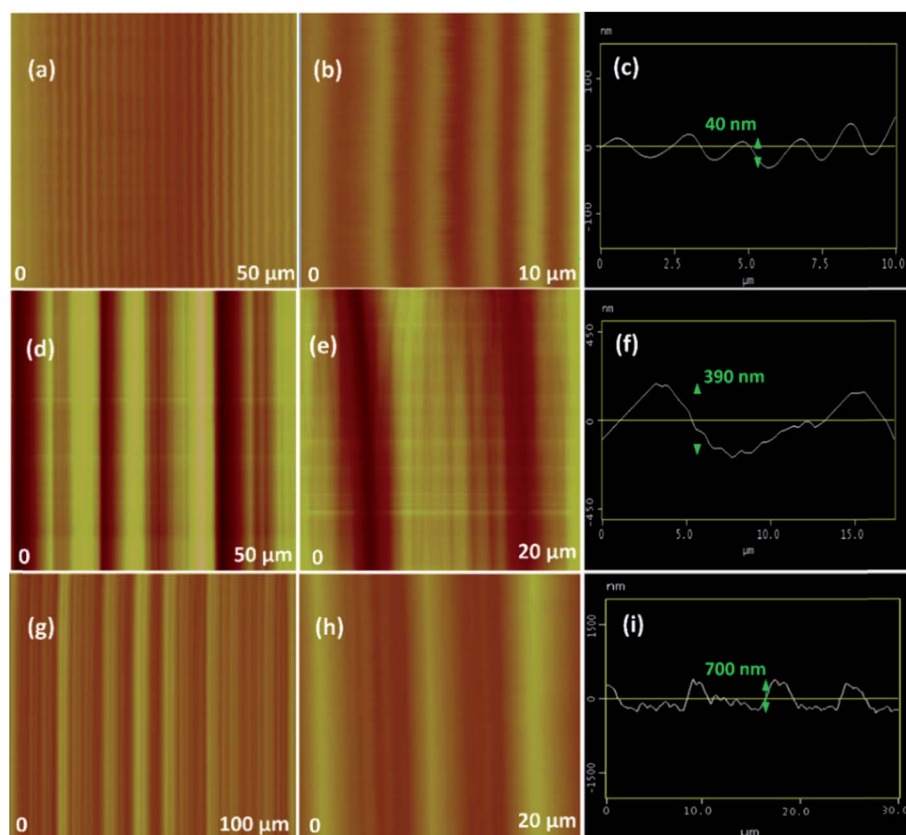


Fig. 2 AFM images and surface profiles for the wrinkles-ridges formed on the surfaces of GO–Au electrode by applying different pre-strains to the PDMS substrate: 2.7% (a–c), 5.1% (d–f), and 8.0% (g–i).

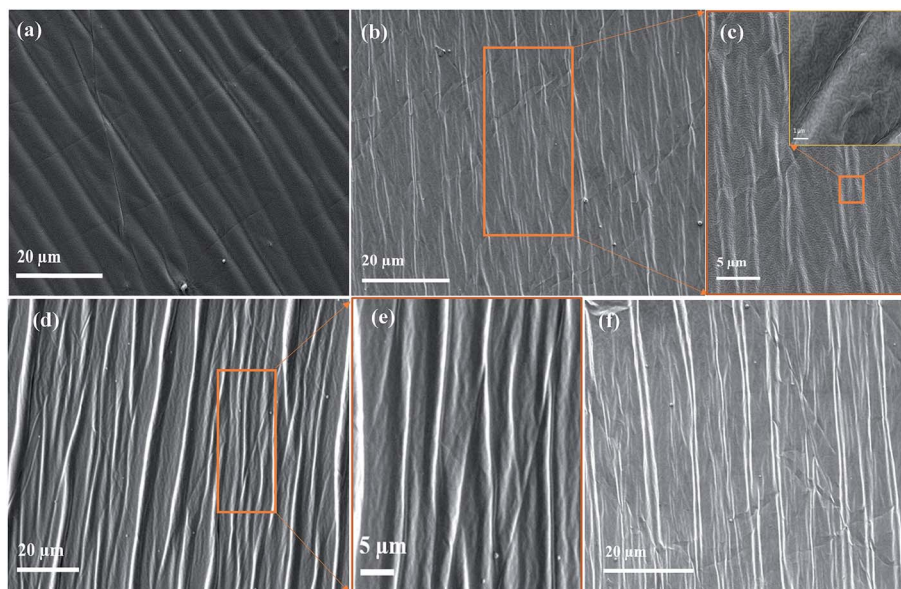


Fig. 3 FESEM images for the wrinkles-ridges formed on the surface of GO–Au electrode by applying different pre-strains to the PDMS substrates: 2.7% (a), 5.1% (b–c), and 8.0% (d–f). The inset of (c) shows the attachment and assembling of GO to the gold surface.

(Fig. 2g–i), the amplitude of localized ridges increased to ~ 700 nm, while their wavelength only slightly reduced. It should be noted that at the high strains of 5.1% and 8%, many small wrinkles also appeared, accompanying with increasing the amplitude of localized ridges. These localized ridges with high amplitude and small wrinkles increase the surface area and roughness compared to the planar film.

The FESEM studies confirm that the wrinkles were formed at the pre-stretch of 2.7% (Fig. 3a) and transformed to localized ridges at 5.1% (Fig. 3b and c), and that with further enhancing the pre-stretch to 8%, the localized ridges became clearer and their amplitude became larger (Fig. 3d–f). The small wrinkles observed by AFM imaging were not clearly seen in SEM imaging due to their small amplitude (~ 40 nm). The inset of Fig. 3c gives shows that the GO nanosheets were assembled on the oxygen plasma treated Au surface. However, some GO nanosheets were found to agglomerate, presumably due to π – π stacking among the single layers.

3.2. Modeling of the morphological transition from wrinkles to localized ridges

The process of wrinkle formation and the subsequent transition to localized ridges can be understood through the following model. In the model, the mode of deformation was assumed to be plane-strain, and the substrate was subject to pre-stretch of various strain levels (2.7%, 3.5%, 5.1%, and 8%). The entire model was compressed horizontally to the point of zero nominal strain in the substrate. Some representative results are plotted in Fig. 4, in which the contour represents the maximum principal strain, and the deformation is shown to scale. The numerical results clearly demonstrate that the appearance of sinusoidal wrinkles at the pre-strain of 2.7% and the transition from sinusoidal wrinkles to localized ridges at the pre-strain of $\sim 3.5\%$. In the cases of even larger pre-strains, more ridges

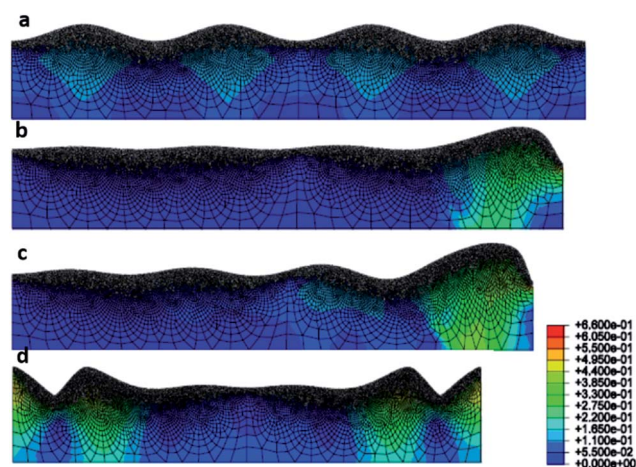


Fig. 4 Simulated results of the surface morphology in a bilayer film–substrate system, in which the substrate was subject to tensile pre-strain of (a) 2.7%, (b) 3.5%, (c) 5.1%, and (d) 8%, and then compressed back. The plots shown are the equilibrium results after full relaxation. The deformed shapes are shown to scale, while the contours show the level of the maximum principal strain.

appear but the characteristic size of each ridge remains almost unchanged. The ridge pattern can be distinguished by the relatively high magnitude and the wide flat regions between neighboring ridges. The ridge instability, as well as the wrinkle–ridge transition, shares some similarity with the ridge patterns observed in single-layer film–substrate systems,^{33,39} but the latter often takes place at a much larger pre-strain. The detailed morphology of the ridges also differs slightly from that observed in single-layer film–substrate systems:³³ here, the aspect ratio of each ridge is not as high, and the ridges often come in pairs, leaving a notch-like groove in between, similar to that observed at a later stage of the period-doubling of wrinkles.⁴⁰

The numerical model suggests that the formation of the ridges at lower pre-stretches and the difference in morphologies could be due to the plasticity of the Au layer. Before yielding, the stiff Au layer acts as a part of the stiff film and wrinkles together with the GO film. When stress exceeds certain level, the Au layer yields. The post-yielding Au appears to be much softer and flows under very small shear stresses. The GO film drifting over the plastic flow of the Au layer can be shifted laterally from the substrate, as if it had delaminated locally.⁴¹ This would explain the earlier emergence of the ridge formation. On the other hand, different from a delaminated state, the GO is still constrained by the Au layer in the vertical direction. This constraint, as well as the relatively low overall strain, explains the lower aspect ratio compared to that formed in single-layer film-substrate systems under large strains.³⁹

3.3. Raman and FTIR structural characterization

The Raman spectroscopic studies confirm the presence of GO nanosheets on the wrinkled surface (Fig. 5a). In spectra, the Au layer does not show any significant Raman peaks. With the incorporation of GO on the surface of Au layer, the peaks for inherent disorder (D) and graphitic (G) bands of GO appear, indicating that the GO nanosheets are well attached to the Au surface. The D-band corresponds to the E_{2g} phonon of sp^2 atoms, while the G-band is known to be the breathing mode of k -point phonon A_{1g} symmetry. The peak position of the D-band at 1351.1 cm^{-1} is caused by out-of-plane vibrations due to presence of structural defects located at the edges of GO nanosheets. The intense peak is due to the disruption of sp^2 bonds of carbon as GO nanosheets have oxidative functional groups, confirming that the GO was assembled on the Au surface. For the samples with the pre-stretches of 2.7% and 5.1%, the peak intensities of the D-band and G-band increases, compared to the planar sample. The value of I_D/I_G is a measure of disorder degree and inversely proportional to the average size of the sp^2 clusters in GO sheets.^{42,43} The result shows that the I_D/I_G ratios at the pre-stretches of 0%, 2.7%, 5.1% and 8.0% are 0.948, 0.930, 0.932, and 0.921, respectively, indicating that there are insignificant changes in the I_D/I_G ratio with varying pre-stretch at the GO-Au-PDMS substrate.

To confirm immobilization of NiR enzyme on the GO surface, we utilized Fourier transform infrared spectroscopy (FTIR) analyses (Fig. 5b). The various peaks in the spectra indicate the presence of carboxylation of GO nanosheets. The vibrational peaks at $3000\text{--}3700\text{ cm}^{-1}$ are attributed to C-OH, -COOH and -H₂O stretching bonds present in the wrinkled GO. The peak at 1780 cm^{-1} is seen due to ketone (C=O) groups at the wrinkled GO sheets. The peak at 1606 cm^{-1} arises due to in-plane stretching (sp^2 -hybridized C=C) of carboxyl groups. The absorption peaks at $1200\text{--}1400\text{ cm}^{-1}$ correspond to epoxy groups (C-O-C).⁴⁴ After the enzyme immobilization, the peak at 1600 cm^{-1} becomes broad and overlapped due to amide I of NiR enzyme molecules. The intensity of peak at 1248 cm^{-1} increases after the enzyme immobilization due to amide II indicating NiR enzyme functionalization on the wrinkled GO surface.

3.4. Electrochemistry

The CV studies of the fabricated electrodes were conducted in phosphate buffered saline (PBS, 50 mM, pH 7.0, 0.9% NaCl) at a potential range of -0.4 V to $+0.6\text{ V}$ (Fig. 6). These electrodes exhibited well-defined oxidation and reduction peaks in presence of redox mediator $[\text{Fe}(\text{CN})_6]^{3-/4-}$. The magnitude of current peak for bare Au-PDMS electrode without pre-stretch was found as $44\text{ }\mu\text{A}$ at an oxidation potential of 0.32 V . After the incorporation of GO nanosheets onto the surface of Au layer, the magnitude of current decreased to $24\text{ }\mu\text{A}$ (Fig. 6a). This is due to oxygenated groups present at the GO surface which obstructs the charge transfer from the redox reaction of $[\text{Fe}(\text{CN})_6]^{3-/4-}$ mediator probe. Interestingly, we obtained higher electrochemical currents in the case of the wrinkled-ridged GO electrodes (Fig. 6b) due to the enhancement of electrochemical surface area for redox reaction to produce sufficient amounts of electrons. Alternately, the transition of the planar (0% pre-stretch) to wrinkled surface (2.7% pre-stretch) may reduce the current conduction path from the bulk solution to the current collector, resulting in a higher current. With increasing pre-stretch from 5.1% to 8.0%, the electrode provides a less current, because more functional groups (-CHO, -COOH, -OH, etc.) existed on the larger active surface area. Upon the attachment of NiR enzyme molecules onto the

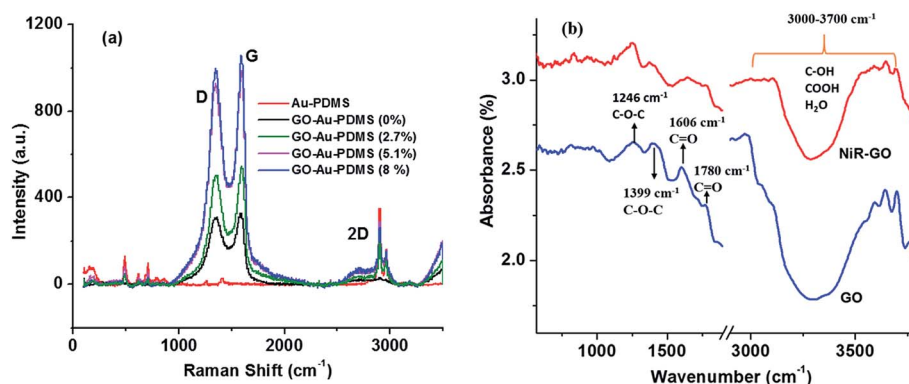


Fig. 5 (a) Raman studies for different wrinkled Au-PDMS substrates (pre-stretch: 0, 2.7%, 5.1%, and 8%) with and without GO nanosheets. (b) FTIR studies for GO-Au-PDMS electrodes before and after enzyme immobilization.

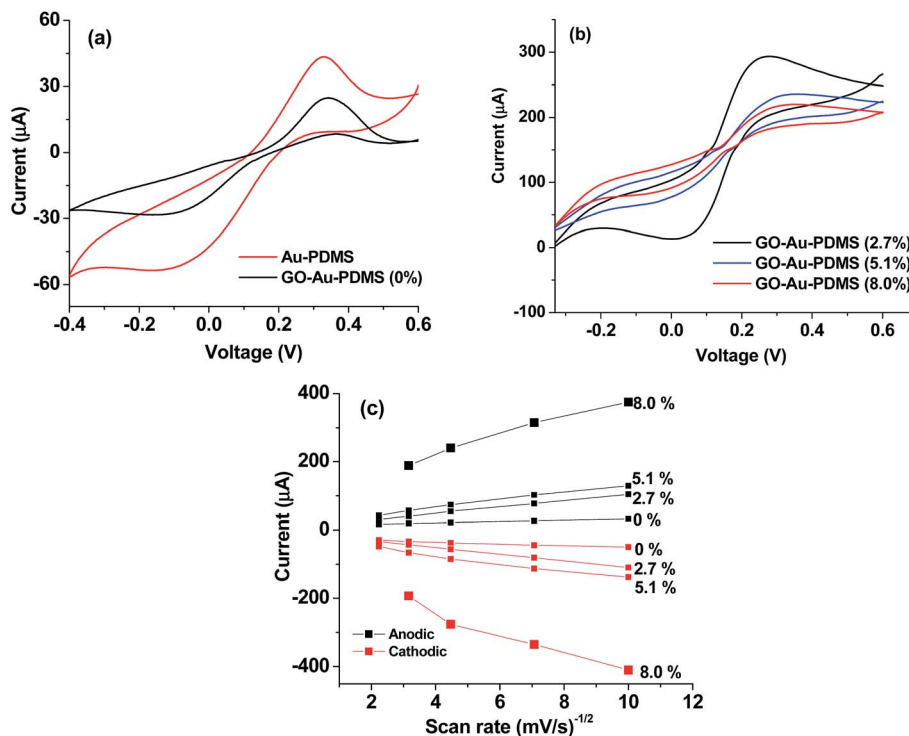


Fig. 6 (a) Overlays of CV for GO–Au–PDMS electrode without pre-stretch. (b) CV curves for wrinkled-ridged GO on Au–PDMS electrodes at different pre-strains: 2.7%, 5.1%, and 8%. The CV studies have been conducted in PBS (50 mM, pH 7.0, 0.9% NaCl) containing 5 mM of $[\text{Fe}(\text{CN})_6]^{3-/4-}$ at a scan rate of 20 mV s^{-1} . (c) Anodic and cathodic peak currents as a function of root mean square of scan rates for the NiR/GO–Au–PDMS bioelectrodes at different pre-strains: 0, 2.7%, 5.1%, and 8%.

wrinkled-ridged GO surfaces, the electrochemical current of electrodes was reduced due to the insulating nature of enzyme, confirming the immobilization NiR molecules on the wrinkled-ridged GO surface (Fig. S2, ESI†).

Cyclic voltammograms for various NiR/GO–Au bioelectrodes (at pre-stretch of 0%, 2.7%, 5.1%, and 8%) as a function of scan rate ($5\text{--}100 \text{ mV s}^{-1}$) are given in Fig. S3 (ESI†). Fig. S3† shows the CV curves of bioelectrodes as a function of pre-stretch from 0% to 8.0%. At the same scan rate of 20 mV s^{-1} for all the bioelectrodes, the peak current was found to increase with increasing pre-stretch and a maximum current was found at the pre-stretch of 8.0% (Fig. S4, ESI†). This may perhaps be due to favorable orientation of enzyme molecules at a higher pre-stretch that may provide a microenvironment for the improvement of heterogeneous electrons transfer through the wrinkled-ridged GO–Au electrode. The anodic and cathodic peak currents were found to be almost proportional and inversely proportional with square root of scan rate, respectively, suggesting a quasi-reversible redox process (Fig. 6c). However, the peak potential shifted towards higher and lower value for the anodic and cathodic peak, respectively, indicating a surface controlled process. The peak current enhancement with increasing scan rate is an indicative of facile electron transfer of the redox moieties deeply embedded into NiR enzyme molecules through the GO nanosheets (Fig. S4†).

To investigate the kinetics of enzymatic activity, we evaluated various electrochemical parameters of the fabricated

bioelectrodes (Table 1). $[\text{Fe}(\text{CN})_6]^{3-/4-}$ redox mediator has been widely used for studying electrochemical parameters of nitrate sensitive bioelectrodes.⁴⁵ In this study, this mediator was chosen to evaluate diffusion coefficient, heterogeneous electron transfer rate constant, and sensitivity of the fabricated bioelectrodes. The surface concentration and diffusion coefficient of all the bioelectrodes for the $[\text{Fe}(\text{CN})_6]^{3-/4-}$ were calculated using eqn (1) and (2).

$$i_p = \frac{n^2 F^2 \nu A \Gamma}{4RT} \quad (1)$$

$$i_p = (2.687 \times 10^5) n^{3/2} A D^{1/2} \nu^{1/2} \Gamma \quad (2)$$

where R , T , n , F , ν , A , D and Γ are the ideal gas constant, the thermodynamic temperature, the number of electrons appearing in half-reaction for the redox couple ($n = 1$), the Faraday constant, the scan rate, the area of the electrode, the diffusion coefficient, and the surface concentration, respectively. The slope of i_p/ν was obtained from the linear regression of the anodic peak current versus the scan rate curves (Fig. S5, ESI†). The diffusion coefficient of a redox species from bulk solution to electrochemical electrode surface is often significantly affected by the shape, size, and material of electrode.^{46–49} For example, Sharma *et al.* reported the influence of the shape of gold nanostructures on the diffusion coefficient of a redox species to electrode surface.⁴⁹ Baur *et al.* also showed different diffusion coefficients of redox couples due to changing the size

Table 1 Comparison of electrochemical parameters for the fabricated tunable NiR/GO–Au bioelectrodes

Pre-stretch ratio	Peak current (μA)	Diffusion coefficient ($\text{cm}^2 \text{s}^{-1}$)	Potential difference ΔE_p (V)	Surface concentration (mol cm^{-2})	Heterogeneous electron transfer rate k_0 (cm s^{-1})	Electrochemical surface area A_{el} ($\text{cm}^2 \times 10^{-5}$)
0%	21.8	1.2×10^{-8}	0.56	1.5×10^{-13}	0.116	0.15
2.7%	53.9	8.1×10^{-8}	0.12	7.9×10^{-13}	0.150	0.22
5.1%	76	1.5×10^{-7}	0.44	9.1×10^{-13}	0.200	0.24
8.0%	239.1	1.6×10^{-6}	0.34	2.1×10^{-12}	0.237	0.834

of disk microelectrodes.⁵⁰ In addition, the diffusion coefficients of ferro/ferricyanide were found as $6.9 \times 10^{-15} \text{ cm}^2 \text{ s}^{-1}$ and $2.26 \times 10^{-10} \text{ cm}^2 \text{ s}^{-1}$ using polyaniline–gold and poly(lactic-co-glycolic acid) encapsulated iron oxide nanoparticles based electrodes, respectively.^{46,47} In our case, without any wrinkles or ridges, the planar NiR/GO–Au bioelectrode shows a low diffusion coefficient of $1.2 \times 10^{-8} \text{ cm}^2 \text{ s}^{-1}$ for $[\text{Fe}(\text{CN})_6]^{3-/4-}$ species from bulk solution to electrode surface. As the pre-stretch increased to 8.0%, the wrinkled-ridged bioelectrode provided more than two orders of magnitude higher diffusion coefficient to $1.6 \times 10^{-6} \text{ cm}^2 \text{ s}^{-1}$ compared to the planar bioelectrode. The higher diffusion coefficient at the pre-stretch of 8.0% may be associated with higher amplitude of localized ridges and small wrinkles of this bioelectrode, contributing to radial diffusion of electrons. A maximum surface concentration of redox mediator $[\text{Fe}(\text{CN})_6]^{3-/4-}$ for the NiR/GO–Au bioelectrode was obtained at the pre-stretch of 8.0% compared to those obtained under other pre-stretching conditions (Table 1). Also, in comparison with the chitosan–TiO₂ (ref. 48) and Au nanostructured electrodes,⁴⁹ the wrinkled-ridged NiR/GO–Au bioelectrodes show a higher surface concentration.

The electrochemical surface area A_{el} of bioelectrode was determined using eqn (3) described in literature⁴⁹ and is given below:

$$A_{\text{el}} = \frac{S}{(2.99 \times 10^5)n^{3/2}D^{1/2}\Gamma} \quad (3)$$

where S is the slope obtained from the linear regression of i_p versus $\nu^{1/2}$ as shown in Fig. 6c. Table 1 also shows the calculated values of A_{el} for the NiR/GO–Au bioelectrodes at different pre-stretch levels and are found to increase with increasing pre-stretch. According to Laviron method, the heterogeneous electron transfer rate constant k_0 and the charge-transfer coefficient α of a surface-controlled redox reaction for the fabricated bioelectrodes were calculated using eqn (4)^{51,52}

$$\log k_0 = \alpha \log(1 - \alpha) + (1 - \alpha) \log \alpha + \log \left(\frac{RT}{nF\nu} \right) - \alpha(1 - \alpha) \frac{nF\Delta E}{2.303 RT} \quad (4)$$

The k_0 values for the NiR/GO–Au electrodes with 2.7%, 5.1% and 8% pre-stretch were found to be higher than that for the planar bioelectrode (Table 1). The formation of wrinkles-ridges at the high pre-stretch of 8.0% may presumably allow for favorable orientation of enzyme molecules on its surface to enhance the

electron transfer ability, thus increasing the value of k_0 . Also, the k_0 values for all the fabricated bioelectrodes are found to be higher compared to that using aminated reduced GO.⁴

3.5. Detection of nitrate ions

We investigated the sensing performance of the fabricated NiR/GO–Au bioelectrodes using CV for detection of nitrate ions (Fig. 7). The nitrate ion concentration was varied from 0 to 1000 μM and the scan rate was fixed at 20 mV s^{-1} . Fig. 7a shows the CV curves for the bioelectrodes with the pre-stretch of 2.7%. The peak current increased with increasing nitrate concentration (see the inset of Fig. 7a). Similarly, for the un-stretched (control) and the other pre-stretched (5.1% and 8%) bioelectrodes, the peak currents during the detection of nitrate ions increased with increasing concentration of nitrate ions (Fig. 7b–d). In the biochemical reaction (Fig. 1), the NiR enzyme molecules on the sensor surface played an important role for generation of electrons. The multiple active sites of the enzyme molecules directly converted NO_3^- to NO_2^- *via* generation of electrons and the generated electron transferred through the wrinkled GO to the Au layer. More nitrate ions in the electrolyte solution created more electrons and the resulting current was directly proportional to the concentration of nitrate ions. Thus, other than mediator electrons from redox reaction, the produced electrons due to the enzymatic reaction were responsible for enhancing electrocatalytic current on the sensor surface. The sensing results (Fig. 7) demonstrate that as the pre-stretch level increased, the bioelectrodes became more sensitive to changes in surrounding nitrate ion concentration. Also, compared to the un-stretched planar bioelectrode, the pre-stretched bioelectrodes provide a wider concentration range of ion detection (Fig. S6, ESI[†]). Table 2 summarizes the sensing performances of all the fabricated bioelectrodes and their comparison with those reported in literature. The comparison indicates that the wrinkled and wrinkled-ridged bioelectrodes offer higher sensitivities compared to those using carbon nanotubes–polypyrrole nanocomposite,⁷ polypyrrole,⁸ platinum–tin,⁹ silver particle–poly-methacrylic acid,¹⁰ and 1-methyl-3-(pyrrol-1-yl-methyl)pyridinium⁴ for electrochemical nitrate detection.

Fig. 8a shows the schematic of the planar and wrinkled-ridged GO with diffusion of generated electrons *via* redox reaction. The planar bioelectrode (0% pre-stretch) is considered with linear diffusion of ions from the bulk solution, providing relatively low diffusivity and sensitivity in the response (Fig. 8b). The wrinkled bioelectrode with the pre-stretch of 2.7% provided

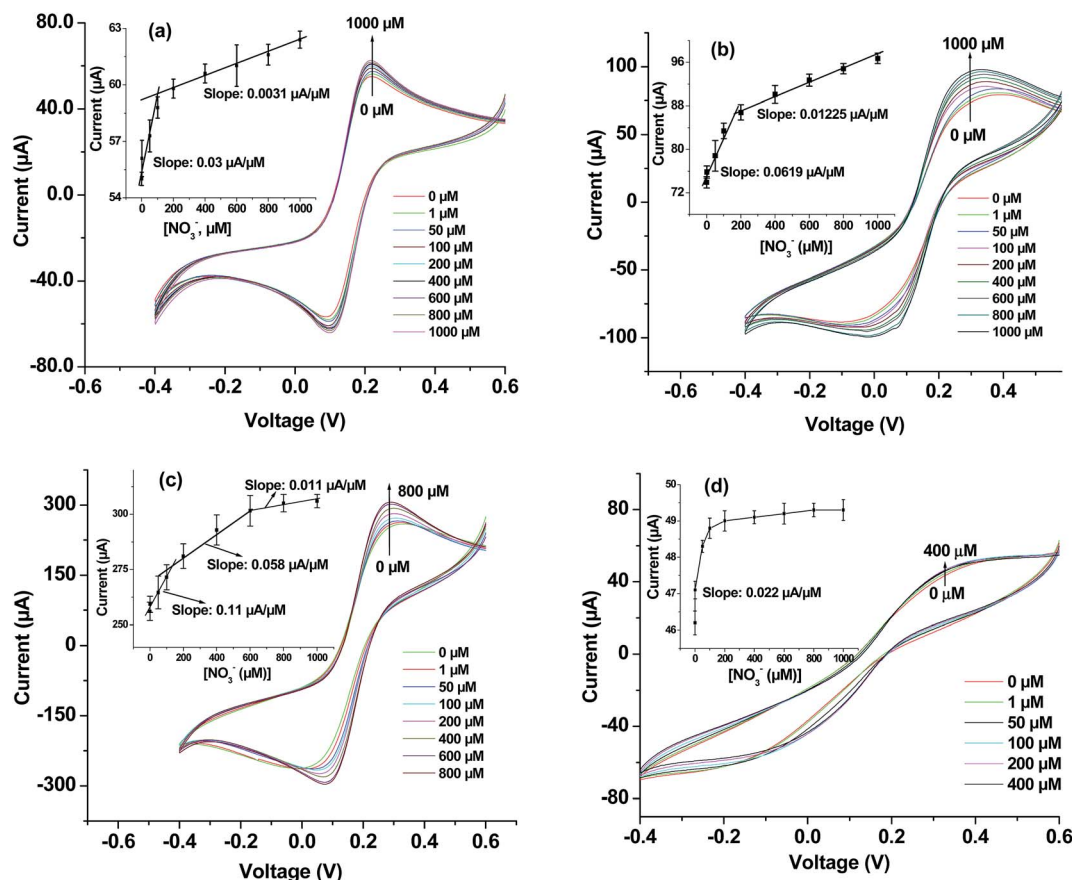


Fig. 7 CV overlays of the fabricated NiR/GO–Au bioelectrodes responding to different nitrate ion concentrations up to 1000 μM at 20 mV s^{-1} . The bioelectrodes were pre-stretched at 2.7% (a), 5.1% (b), and 8.0% (c). The control bioelectrode in (d) was un-stretched (0%). Insets show the sensor calibration plots as a function of nitrate ion concentration. The error bars in each inset were obtained by taking the standard deviation of three measurements at each concentration.

Table 2 Sensing performances for the fabricated tunable NiR/GO–Au bioelectrodes (area: 7 mm \times 7 mm) and their comparison with other electrochemical nitrate sensors reported in literature

Electrodes	Methods	Test range (μM)	Linear range (μM)	Sensitivity ($\mu\text{A L mol}^{-1} \text{cm}^{-2}$)	Regression coefficient (r^2)	Ref.
1-Methyl-3-(pyrrol-1-yl-methyl)pyridinium	Amperometry	100	100	0.078	NA	4
CNT–polypyrrole	Amperometry	440–1450	440–1450	0.0003	NA	7
Polypyrrole	Potentiometry	50–5000	NA	NA	0.992	8
Platinum–tin	Linear sweep voltammetry	0–806	16–322	0.0064	0.998	9
Silver particle–polymethacrylic-acid	Cyclic voltammetry	0–20 000	NA	0.130	NA	10
Methyl viologen/Nafion	Conductance	20–500	20–250	NA	0.997	53
GO–Au (0% pre-stretch)	Cyclic voltammetry	1–1000	1–100	0.044	0.920	This work
GO–Au (2.7% pre-stretch)		1–1000	1–100	0.061	0.963	
			100–1000	0.0063	0.994	
GO–Au (5.1% pre-stretch)		1–1000	1–200	0.126	0.970	
			200–1000	0.025	0.993	
GO–Au (8.0% pre-stretch)		1–1000	1–100	0.224	0.982	
			100–600	0.118	0.983	
			600–1000	0.023	0.980	

an improved sensitivity due to higher diffusivity. This may be a consequence of the wrinkle formation on the electrode surface that leads to a larger electroactive surface area for loading more

enzyme molecules to participate in catalytic reactions.⁵⁴ These wrinkles also act as microelectrodes to enhance mass transport of ions to and from the electrode surface by providing spherical

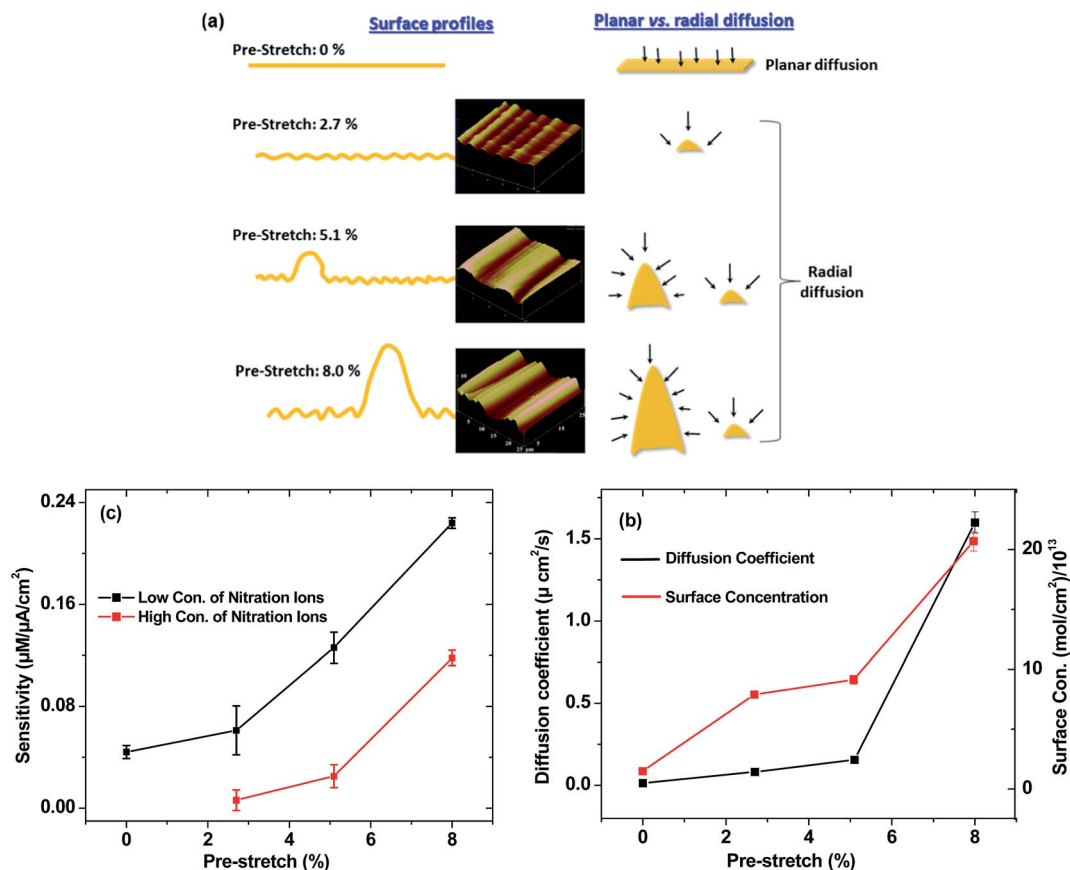


Fig. 8 (a) Pictorial representation for diffusion of ions occurring on the surface of NiR/GO–Au bioelectrodes. Insets show the AFM 3D profiles of the surfaces. (b) Diffusion coefficient and surface concentration for NiR/GO–Au bioelectrodes as a function of pre-stretch value. (c) Sensitivity as a function of pre-stretch level at lower (0–100 μM for both 2.7% and 8% pre-stretch, and 0–200 μM for 5.1% pre-stretch) and higher (100–1000 μM for 2.7% pre-stretch, 200–1000 μM for 5.1% pre-stretch, and 200–600 μM for 8% pre-stretch) concentrations of nitrate ions (also, refer to Table 2 for the lower and higher concentration ranges of nitrate ions). The error bars in (b) and (c) were obtained by taking the standard deviation of three measurements at each pre-stretch.

or radial diffusion from multiple directions in the surrounding bulk solution. In fact, spherical or radial diffusion of a redox-active species at microelectrode surface has been extensively demonstrated to generate a concentration gradient between the electrode surface and bulk solution.^{54–58}

Alternately, the edge planes of wrinkled GO may provide higher charge transfer kinetics compared to other nanostructured materials^{4,59} resulting in higher sensitivity. At the pre-stretch of 5.1%, the transition from sinusoidal wrinkles to localized ridges influenced the electrochemical performance of the sensor (Fig. 8a). Both ion diffusivity and surface concentration increased (Fig. 8b) presumably due to the appearance of larger amplitude of the ridges that further enhances the electroactive surface area. In addition, the small wrinkles partially contributes to accepting more electrons generated from the electrochemical reaction *via* radial diffusion, resulting in an improved sensitivity. At the pre-stretch of 8%, the amplitude of localized ridges increased, thus further increasing electro-active surface area (Fig. 8a). Thus, the morphological change on the surface of the bioelectrodes with 8% pre-stretch led to higher diffusion and surface concentration towards a higher sensitivity (Fig. 8c).

In the control studies, GO nanosheets were assembled on the planar Au–PDMS surface. A lower sensitivity (0.044 $\mu\text{A L mol}^{-1} \text{cm}^{-2}$) was found for the control sensor compared to the other sensors with the pre-stretch substrate (Fig. 7d). The current response of the control sensor was almost saturated after 100 μM concentration of nitrate ions. The current *versus* concentration plots of all the fabricated biosensors are shown in Fig. S6 (ESI[†]). These results show that the formation of wrinkles and ridges on the sensor surface (at 8% pre-stretch) could not only improve sensitivity, but also provide a higher detection range up to 800 μM of nitrate concentration. In comparison, a Nafion-coated glassy carbon electrode and a thin anion-permselective coating of 1-methyl-3-(pyrrol-1-yl-methyl)pyridinium across the surface of a microporous support membrane were reported to detect up to 140 μM and 100 μM of nitrate ions, respectively.⁴ While a bienzyme functionalized polypyrrole film was able to detect nitrate ions in a range of 100–5000 μM ,² its sensitivity was relatively low.

The effect of potential interfering ions for all the fabricated bioelectrodes was investigated. As it is almost impossible to test the sensors with all possible interfering ions, only a few sample ions were tested to demonstrate selectivity of the bioelectrodes,

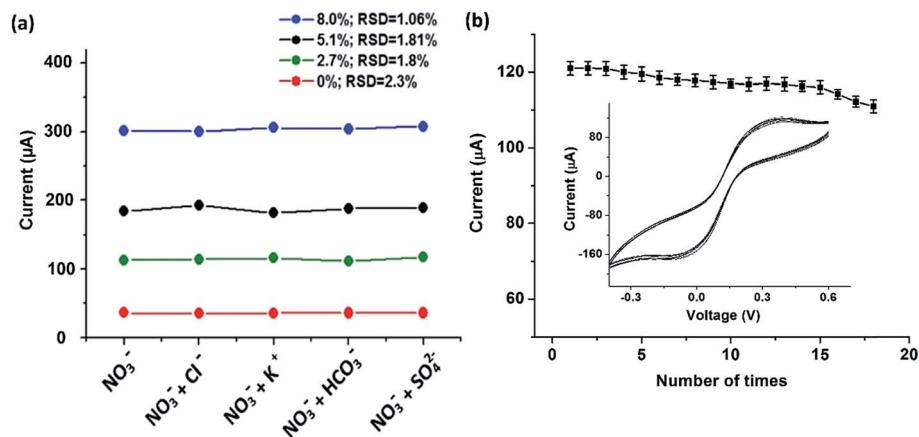


Fig. 9 (a) Current responses of the nitrate sensitive bioelectrodes (at pre-stretch values of 0%, 2.7%, 5.1%, and 8.0%) to some sample interfering ions. The ion concentration of Cl^- , K^+ , HCO_3^- , and SO_4^{2-} were 450 μM , 200 μM , 100 μM , and 50 μM , respectively. These interfering ions were mixed with 100 μM nitrate ions. (b) Current response for stability test of NiR/GO–Au–PDMS bioelectrode (pre-stretch: 8.0%) as a function of number of times in presence of 50 μM nitrate concentration. Inset shows corresponding CV curves at scan rate of 10 mV s^{-1} .

including SO_4^{2-} , K^+ , Cl^- , and HCO_3^- . We utilized 100 μM concentration of nitrate ions mixed with one of the interfering ions for selectivity measurements. The CV measurements (Fig. S7, ESI[†]) were conducted at the scan rate of 20 mV s^{-1} . The current responses of the bioelectrodes are shown in Fig. 9a. All the bioelectrodes show good selectivity in presence of these interfering ions as evident by their low relative standard deviation (RSD) of the current. This is because the enzyme (NiR) molecules covalently attached on the surface of GO do not allow reducing oxo-compounds, such as sulfate, nitrite, and chlorate.

To test reproducibility of the proposed bioelectrode, we fabricated six identical NiR/GO–Au bioelectrodes, all with 8.0% pre-stretch. The resulting wrinkled-ridged bioelectrodes were tested by adding 50 μL amount of nitrate ions (100 μM) using the CV technique at 10 mV s^{-1} . The low RSD of peak current at the level of $\pm 4.5\%$ indicates that the bioelectrodes had good reproducibility. Furthermore, the stability for the bioelectrode (8.0% pre-stretch) was investigated using CV studies for repeated measurements. Fig. 9b shows the CV curves of 18 times repeated measurements where the inset gives the corresponding peak currents obtained as a function of repeated times. The response of this wrinkled-ridged bioelectrode was found to 94.2% within 15 repeated CV measurements after which it was reduced to 91.7% from the initial signal. The RSD value for the 18 repeated CV measurements was $\pm 2.79\%$.

4. Conclusions

In conclusion, we demonstrated the controlled formation of microscale wrinkles and localized ridges on the surface of GO–Au–PDMS composite to tune and optimize the sensing performance of the electrochemical nitrate sensors. Nitrate reductase was exploited for covalent immobilization on the GO surface. By simply varying pre-stretch values of the elastomer, the shape and size of wrinkles and localized ridges were tuned, thus changing the electrochemical current and sensing characteristics of the bioelectrode. With increasing pre-stretch of the

elastomer, the sinusoidal wrinkles were transformed to localized ridges after complete relaxation. Due to an increase in electroactive surface area with radial diffusion, the wrinkled-ridged NiR/GO–Au bioelectrode exhibited an improved diffusivity of electrons generated from catalytic reaction, a higher electron transfer rate, and a higher surface concentration, thus resulting in a higher sensitivity of $0.224 \mu\text{A } \mu\text{M}^{-1} \text{ cm}^{-2}$, approximately five times higher than that of the planar counterpart bioelectrode. The present sensor also demonstrated excellent selectivity in presence of some sample ions such as SO_4^{2-} , K^+ , Cl^- , and HCO_3^- . Further work includes integrating the developed wrinkled bioelectrodes into microfluidic channels to form microfluidic nitrate sensors. In addition, it is worthwhile to study using other redox mediators such as ruthenium hexamine and ferrocene derivatives to improve performance of the sensors in the future.

Acknowledgements

This work was supported in part by the Iowa State University's Plant Sciences Institute, the Iowa Corn Promotion Board, the U.S. National Science Foundation under grants CCF-1331390, DBI-1353819, and DGE-1545453. The authors also thank Dr Chenxu Yu and Chao Wang for Raman measurement and Dr Warren Straszheim for SEM measurement.

References

- W. Xuejiang, V. D. Sergei, J.-M. Chovelon, N. J. Renault, C. Ling, X. Siqing and Z. Jianfu, *Talanta*, 2006, **69**, 450–455.
- M. Sohail and S. B. Adeloju, *Sens. Actuators, B*, 2008, **133**, 333–339.
- D. Silva, S. D. Shan and S. Cosnier, *Sens. Actuators, B*, 2004, **103**, 397–402.
- L. M. Moretto, P. Ugo, M. Zanata, P. Guerriero and C. R. Martin, *Anal. Chem.*, 1998, **70**, 2163–2166.

- 5 N. Adarsh, M. Shanmugasundaram and D. Ramaiah, *Anal. Chem.*, 2013, **85**, 10008–10012.
- 6 W. L. Daniel, M. S. Han, J.-S. Lee and C. A. Mirkin, *J. Am. Chem. Soc.*, 2009, **131**, 6362–6363.
- 7 F. Can, S. K. Ozoner, P. Ergenekon and E. Erhan, *Mater. Sci. Eng., C*, 2012, **32**, 18.
- 8 M. Sohail and S. B. Adeloju, *Electroanalysis*, 2009, **21**, 1411–1418.
- 9 Y. Fu, C. Bian, J. Kuang, J. Wang, J. Tong and S. A. Xia, *Sensors*, 2015, **15**, 23249.
- 10 S. G. Leonardi, N. Donato, A. Bonavita, G. Neri, M. Bonyani and A. Mirzaei, *IEEE InAISEM Ann. Conf.*, 2015, pp. 1–4.
- 11 K. Kostarelos and K. S. Novoselov, *Nat. Nanotechnol.*, 2014, **9**, 274.
- 12 Z. Tehrani, G. Burwell, M. A. M. Azmi, A. Castaing, R. Rickman, J. Almarashi, P. Dunstan, A. M. Beigi, S. H. Doak and O. J. Guy, *2D Materials*, 2014, **1**, 025004.
- 13 W. Park, J. M. Yoon, M. Park, J. Lee, S. K. Kim, J. W. Jeong, K. Kim, H. Y. Jeong, S. Jeon, K. S. No, J. Y. Lee and Y. S. Jung, *Nano Lett.*, 2012, **12**, 1235–1240.
- 14 C. Gómez-Navarro, R. T. Weitz, A. M. Bittner, M. Scolari, A. Mews, M. Burghard and K. Kern, *Nano Lett.*, 2007, **7**, 3499–3503.
- 15 F. Bonaccorso, Z. Sun, T. Hasan and A. C. Ferrari, *Nat. Photonics*, 2010, **4**, 611–622.
- 16 J. T. Robinson, F. K. Perkins, E. S. Snow, Z. Wei and P. E. Sheehan, *Nano Lett.*, 2008, **8**, 3137–3140.
- 17 H. Gwon, H.-S. Kim, K. U. Lee, D.-H. Seo, Y. C. Park, Y.-S. Lee, B. T. Ahn and K. Kisuk, *Energy Environ. Sci.*, 2011, **4**, 1277–1283.
- 18 D. R. Dreyer, S. Park, C. W. Bielawski and R. S. Ruoff, *Chem. Soc. Rev.*, 2010, **39**, 228–240.
- 19 Y. Zhu, S. Murali, W. Cai, X. Li, J. W. Suk, J. R. Potts and R. S. Ruoff, *Adv. Mater.*, 2010, **22**, 3906–3924.
- 20 Z. Wen, X. Wang, S. Mao, Z. Bo, H. Kim, S. Cui and J. Chen, *J. Adv. Mater.*, 2012, **24**, 5610–5616.
- 21 M. F. El-Kady, V. Strong, S. Dubin and R. B. Kaner, *Science*, 2012, **335**, 1326–1330.
- 22 J. H. Jung, D. S. Cheon, F. Liu, K. B. Lee and T. S. Seo, *Angew. Chem., Int. Ed. Engl.*, 2010, **49**, 5708–5711.
- 23 P. Zhang, X. Chai, C. Xu and J. Zhou, *IEEE 9th Internation. Conf., ASIC (ASICON)*, 2011, pp. 653–656.
- 24 H. A. Becerril, J. Mao, Z. Liu, R. M. Stoltenberg, Z. Bao and Y. Chen, *ACS Nano*, 2008, **2**, 463–470.
- 25 O. C. Compton and S. T. Nguyen, *Small*, 2010, **6**, 711–723.
- 26 T. Chen, Y. Xue, A. K. Roy and L. Dai, *ACS Nano*, 2013, **8**, 1039–1046.
- 27 B. G. Choi, H. Park, T. J. Park, M. H. Yang, J. S. Kim, S. Y. Jang, N. S. Heo, S. Y. Lee, J. Kong and W. H. Hong, *ACS Nano*, 2010, **4**, 2910–2918.
- 28 V. Mani, A. P. Periasamy and S.-M. Chen, *Electrochem. Commun.*, 2012, **17**, 75–78.
- 29 L. Tang, H. Feng, J. Cheng and J. Li, *Chem. Commun.*, 2010, **46**, 5882–5884.
- 30 N. G. Shang, P. Papakonstantinou, M. McMullan, M. Chu, A. Stamboulis, A. Potenza, S. S. Dhesi and H. Marchetto, *Adv. Funct. Mater.*, 2008, **18**, 3506–3514.
- 31 S. H. Ahn and L. J. Guo, *Nano Lett.*, 2010, **10**, 4228–4234.
- 32 T. Ohzono, H. Watanabe, R. Vendamme, C. Kamaga, T. Kunitake, T. Ishihara and M. Shimomura, *Adv. Mater.*, 2007, **19**, 3229–3232.
- 33 J. Zang, X. Zhao, Y. Cao and J. W. Hutchinson, *J. Mech. Phys. Solids*, 2012, **60**, 1265–1279.
- 34 L. Jin, A. Takei and J. W. Hutchinson, *J. Mech. Phys. Solids*, 2015, **81**, 22–40.
- 35 J. Y. Chung, A. J. Nolte and C. M. Stafford, *Adv. Mater.*, 2011, **23**, 349–368.
- 36 K. Efimenko, M. Rackaitis, E. Manias, A. Vaziri, L. Mahadevan and J. Genzer, *Nat. Mater.*, 2005, **4**, 293–297.
- 37 J. A. Rogers, T. Someya and Y. Huang, *Science*, 2010, **327**, 1603–1607.
- 38 T. Ma, H. Liang, G. Chen, B. Poon, H. Jiang and H. Yu, *Opt. Express*, 2013, **21**, 11994–12001.
- 39 C. Cao, H. F. Chan, J. Zang, K. W. Leong and X. Zhao, *Adv. Mater.*, 2014, **26**, 1763–1770.
- 40 L. Pocivavsek, R. Dellis, A. Kern, S. Johnson, B. Lin, K. Y. C. Lee and E. Cerda, *Science*, 2008, **320**, 912–916.
- 41 Q. Wang and X. Zhao, *Sci. Rep.*, 2015, **5**, 8887.
- 42 O. Akhavan and E. Ghaderia, *Carbon*, 2012, **50**, 1853–1860.
- 43 S. Pei and H.-M. Cheng, *Carbon*, 2012, **50**, 3210–3228.
- 44 M. Acik, G. Lee, C. Mattevi, A. Pirkle, R. M. Wallace, M. Chhowalla and Y. Chabal, *J. Phys. Chem. C*, 2011, **115**, 19761–19781.
- 45 B. Strehlitz, B. Gründig, W. Schumacher, P. M. Kroneck, K. D. Vorlop and H. Kotte, *Anal. Chem.*, 1996, **68**, 807–816.
- 46 A. Soni, C. M. Pandey, S. Solanki and G. Sumana, *RSC Adv.*, 2015, **5**, 45767–45774.
- 47 C. M. Pandey, I. Tiwari and G. Sumana, *RSC Adv.*, 2014, **4**, 31047–31055.
- 48 M. A. Ali, S. Srivastava, K. Mondal, P. M. Chavhan, V. V. Agrawal, R. John, A. Sharma and B. D. Malhotra, *Nanoscale*, 2014, **6**, 13958–13969.
- 49 S. Rachna, V. V. Agrawal, A. K. Srivastava, L. Nain, M. Imran, S. R. Kabi, R. K. Sinha and B. D. Malhotra, *J. Mater. Chem. B*, 2013, **1**, 464–474.
- 50 J. E. Baur and R. M. Wightman, *J. Electroanal. Chem. Interfacial Electrochem.*, 1991, **305**, 73–81.
- 51 A. L. Eckermann, D. J. Feld, J. A. Shaw and T. J. Meade, *Coord. Chem. Rev.*, 2010, **54**, 1769–1802.
- 52 M. A. Ali, K. K. Reza, S. Srivastava, V. V. Agrawal, R. John and B. D. Malhotra, *Langmuir*, 2014, **30**, 4192–4201.
- 53 X. Wang, S. V. Dzyadevych, J. M. Chovelon, N. J. Renault, L. Chen, S. Xia and J. Zhao, *Electrochem. Commun.*, 2006, **8**, 201–205.
- 54 N. Godino, X. Borriose, F. X. Munoz, F. J. del Campo and R. G. Compton, *J. Phys. Chem. C*, 2009, **113**, 11119–11125.
- 55 R. J. Forster, *Chem. Soc. Rev.*, 1994, **23**, 289–297.
- 56 J. Heinze, *Angew. Chem., Int. Ed.*, 1991, **30**, 170–171.
- 57 M. Pumera, *Nanomaterials for Electrochemical Sensing and Biosensing*, CRC Press, 2014.
- 58 T. J. Davies and R. G. Compton, *J. Electroanal. Chem.*, 2005, **585**, 63–82.
- 59 S. A. Glazier, E. R. Campbell and W. H. Campbell, *Anal. Chem.*, 1998, **70**, 1511–1515.